Scholars Journal of Engineering and Technology

OPEN ACCESS

Abbreviated Key Title: Sch J Eng Tech
ISSN 2347-9523 (Print) | ISSN 2321-435X (Online)
Journal homepage: https://saspublishers.com

Estimation of Angle of Attack in Satellite Launch Vehicle Using Flush Air Data Sensing Systems at Mach 0.5 to 3.0

R. C. Mehta[1*]

[1]Professor, Department of Aeronautical Engineering, Noorul Islam Centre for Higher Education, Kumaracoil, 629180, India

DOI: 10.36347/sjet.2021.v09i07.001 | **Received:** 26.06.2021 | **Accepted:** 29.07.2021 | **Published:** 01.08.2021

***Corresponding author:** R. C. Mehta

Abstract **Review Article**

This paper presents an inverse analysis to estimate angle of attack during ascent period of a satellite launch vehicle. Aerodynamic results are numerically computed by solving three dimensional, time dependent, compressible inviscid equations over payload shroud of a satellite launch vehicle. The flush air data system consists of four pressure ports flushed with conical-nose section of the payload fairing and connected to on board differential pressure transducers. The inverse algorithm uses calibrations charts which based on computed and measured data. A controlled random search method is used to predict pitch, yaw and total angle of attack of vehicle from measured transient differential pressure history in flight from Mach numbers range of 0.5 to 3.0. The algorithm predicts the flow direction stepwise with function of flight Mach numbers and can be termed as online method. Flow direction of the launch vehicle is compared with the reconstructed trajectory data. The estimated values of the flow direction are found in good agreement them.

Keywords: aerodynamic; angle of attack; computational fluid dynamics; compressible flow; flush air data system; controlled random search; inverse problem; satellite launch vehicle.

1. INTRODUCTION

Angle of attack of the vehicle in pitch and yaw planes in the ascent phase of a satellite launch vehicle are important parameters to assess the health and behaviour of the vehicle during transonic speed and maximum dynamic pressure regime. Using angle of attack data, instantaneous structural loads, wind and effects of transonic buffeting etc. can be checked and verified with the aerodynamic design as well as expansion of the flight envelope. It is proposed here to use an flush mounted pressure transduces to measure the angle of attach and sideslip angle, along with other basic aerodynamic parameters such as Mach number, dynamic, static and stagnation pressure, throughout transonic to supersonic Mach numbers range. The vehicle loads are the greatest in the transonic flight regime.

Angle of attack and sideslip angle is important parameters in the post-flight reconciliation of flight measurements with ground based experiments and computational fluid dynamics (CFD) prediction. On board inertial measurement units are used to compute vehicle velocity with respect to a fixed coordinate system in conjunction with trajectory of the vehicle. The determination of air data is a technique based on flowfield pressure measurement consists of a number of pressures tapings flush with vehicle surface, usually near the blunt-nose. The measured distribution of the pressure field around the nose is then used to infer the air data. A minimum of four pressure ports are required to obtain a complete set of air data parameters.

Two types of pressure probes mounting, one is fuselage body and the other one is blunt forebody mounting with an aerospike because the flush air data system (FADS) is sensitive to pressure port location. The difference of measured pressure on the wedge or cone surfaces [1] can be related to flow conditions by employing oblique shock relations and conical shock charts, respectively. Larson *et al*., [2] used wind tunnel data to study FADS performance of vehicle at Mach numbers from 0.7 to 1.4. They evaluated freestream values of stagnation pressure, static pressure, angle of attack, angle of sideslip, and Mach number from FADS. An aerospike is employed on the external tank of space shuttle to measure angle of incidence during the ascent phase of the flight [3]. In the post flight analysis the measured pressure obtained through the telemetry are used to estimate angle of attack and sideslip angle in conjunction with wind tunnel data.

Aerodynamic characteristics of hypersonic vehicle are evaluated employing flight data by Watanbe *et al*., [4]. Design and calibration of FADS of the X-33 has been performed by Whitmore *et al*., [5]. Cobleigh *et al*., [6] calibrated FADS pressure model and solution algorithm of a sphere, spherical cones, a Rankine half-body, and the F-14, F/A-18, X-33, X-34, and X-38 configurations. Johnson *et al*., [7] have conducted experimental and numerical simulation of flow field over a forebody of HYFLEX vehicle. It has been shown by them that CFD provides a quick and inexpensive way to calibrate the air data system and is applicable to a broad range of flight conditions. FADS on a sharped-nosed body for Mach 3 to 8 has been developed by Davis *et al*., [8]. Fan *et al*., [9] used neural network based calibration technique to evaluate aerodynamic of multi-hole pressure probes. Rohlf *et al*., [10] carried out vector identification of X-31using FADS. Neural network based flush air data system has been applied on a mini air vehicle by Samy *et al*., [11]. They found that the CFD simulations are useful to identify the ideal pressure port locations. Baumann *et al*., [12] applied FADS to analyze test results of X-43A. Paces *et al*., [13] analyzed angle of attack and sideslip angle using twin differential sensor modules. FADS have been applied to evaluate the performance of UAV by Quindlen *et al*., [14]. Comparative study on solving various flush air data system has been presented by Liu *et al*., [15]. Chen *et al*., [16] studied the FADS of hypersonic vehicle using an algorithm based on neural network. Srivastava and Meade [17] carried out comprehensive probabilistic frame work to learn air data from surface pressure measurements. Karlguard *et al*., [18] coupled inertial navigation and FADS algorithm for estimation atmospheric estimation. Shevchenko and Shmakov [19] have evaluated multi-hole probes in wind-tunnel experiments in conjunction with FADS. Reis *et al*., [20] applied optimization of aerodynamic for airfoil inverse design. It shows that a large number of research papers are appeared for analysis of flow using FADS in conjunction with neural network algorithm. The calibration requires a large data base to train multi-layer neural network to predict the aerodynamic characteristic of vehicle.

Correction factors may be obtained from wind-tunnel tests but these may not cover the entire flight envelope. Using a validated CFD flow solver to generate a suite of correction factors is an attractive option due to its wide range of applicability, low cost, and very high precision. Anderson *et al*., [21] have used finite volume flux splitting method to solve compressible Euler equations. Computed results of inviscid flow field around aerospace vehicles have been compared with experimental and flight data by An *et al*., [22]. Literature survey reveals that the three-dimensional compressible Euler equations are used to compute flowfield over launch vehicles. Their prediction of aerodynamic characteristics based on wind-tunnel test results and numerical data are employed for Mach numbers from 2 to 14.

In this paper, a study of inverse analysis using controlled random search (CRS) algorithm is applied to estimate angle of attack, sideslip angle and total angle of attack of a typical satellite launch vehicle as shown in Fig-1. Pressure ports are located x/D = 0.77. Angle of attack α and sideslip angle β are exhibited in the schematic sketch of the vehicle. The three-dimensional Euler equations are used for computation of pressure distribution for freestream Mach numbers range 0.5 to 3.0 and at angles of attack ± 8°. Pressure data were then converted to the desired air data through calibration data curve. Differential pressure measurement on a conical region of payload fairing is employed to estimate angle of attack and sideslip angle of the satellite launch vehicle

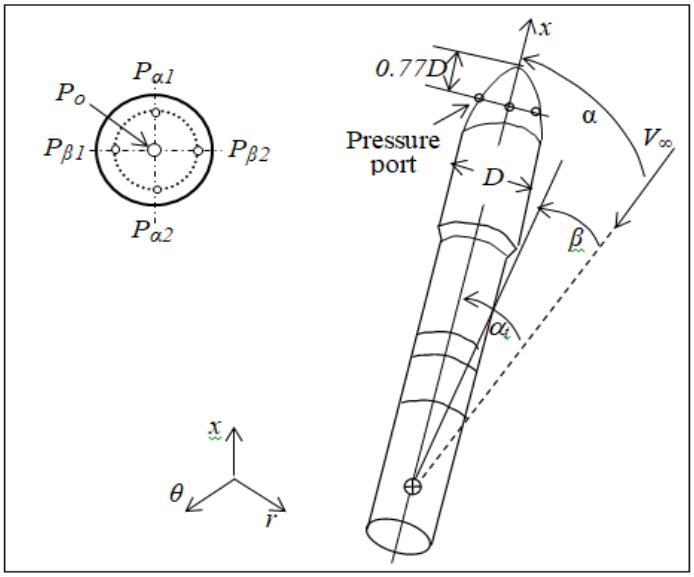

Fig-1: Schematic sketch of satellite launch vehicle

2. NUMERICAL ANALYSIS

2.1 Governing equations

The variation of normal pressure across the blunt-cone region of payload fairing is considered negligible because no flow separation is allowed in this region. The fluid motion of governed by time dependent three-dimensional compressible inviscid equations for the ideal gas which express the conservation of mass, momentum and energy in the absence of external forces. The high-speed flow over the payload fairing is are expressed by the cylindrical form of the Euler equations [23] of motion in a flux vector form as

$$\frac{\partial \boldsymbol{U}}{\partial t}+\frac{\partial \boldsymbol{E}}{\partial x}+\frac{\partial \boldsymbol{F}}{\partial r}+\frac{\partial \boldsymbol{G}}{\partial \theta}+\boldsymbol{H}=0 \quad \ldots\ldots\ldots\ldots\ldots\ldots (1)$$

Where **U** is conservative vector fluxes, the convective vector **E**, **F** and **G** are inviscid flux vector and the source term **H** are defined as

$$\boldsymbol{U}=\begin{bmatrix}\rho\\ \rho v_x\\ \rho v_r\\ \rho v_\theta\\ \rho e\end{bmatrix},\ \boldsymbol{E}=\begin{bmatrix}\rho v_x\\ \rho v_x^2+p\\ \rho v_x v_r\\ \rho v_x v_\theta\\ (\rho e+p)v_x\end{bmatrix},\ \boldsymbol{F}=\begin{bmatrix}\rho v_r\\ \rho v_r v_x\\ \rho v_r^2+p\\ \rho v_r v_\theta\\ (\rho e+p)v_r\end{bmatrix},\ \boldsymbol{G}=\frac{1}{r}\begin{bmatrix}\rho v_\theta\\ \rho v_\theta v_x\\ \rho v_\theta v_r\\ \rho v_\theta^2+p\\ (\rho e+p)v_\theta\end{bmatrix},\ \boldsymbol{H}=\frac{1}{r}\begin{bmatrix}\rho v_r\\ \rho v_r v_x\\ \rho\left(v_r^2-v_\theta^2\right)\\ 2\rho v_r v_\theta\\ (\rho e+p)v_r\end{bmatrix} \quad \ldots. (2)$$

Where v_x, v_r, v_θ are the velocity components in the x, r and θ directions, respectively. T is related to p and ρ by perfect gas equation of state as

$$p=(\gamma-1)\left[e+\frac{1}{2}\rho\left(v_x^2+v_r^2+v_\theta^2\right)\right] \quad \ldots\ldots\ldots\ldots (3)$$

The ratio of the specific heat γ was assumed constant value and γ = 1.4.

2.2 Numerical flow solver

To simplify the spatial discretization in numerical technique, Eq. (1) can be written in the integral form over a finite computational domain Ω with the boundary Γ as

$$\int_\Omega \boldsymbol{U}d\Omega+\int_\Gamma(\boldsymbol{E}+\boldsymbol{F}+\boldsymbol{G})d\Gamma=\int_\Omega \boldsymbol{H}d\Omega \quad \ldots\ldots. (4)$$

Here Ω is a control volume with surface Γ. The contour integration around the boundary of the cell is performed in anticlockwise sense in order to keep flux vectors normal to boundary of the cell. The computational domain has a finite number of non-overlapping hexahedral cells. In a cell centred finite volume method, the flux variables are stored at the centroid of the grid cell and the control volume is formed by the cell itself. The conservation variables within the computational cell are represented by their average values at the cell centre.

The inviscid fluxes are computed at the cell-centre resulting in flux balance. The summation is carried out over the eight edges of the cell. The space discretization scheme shares the reconstruction of the conservative variables of cell interfaces but differ in the evaluation of fluxes in time stepping. The inviscid fluxes are obtained from Roe's approximate Reimann solver. The spatial discretization described above reduces the integral equation to semi-discrete ordinary differential equations. The numerical algorithm is second-order accurate in space discretization and time integration. The numerical scheme is stable for a Courant number ≤ 2. Local time steps are used to accelerate to a steady-state solution by setting the time-step at each point to the maximum value allowed by the local Courant-Friedrichs-Lewy (CFL) condition.

2.3 Initial and boundary conditions

To solve the equations of motion, one has to have the initial boundary conditions, which defines a particular problem. At the inflow, all the flow variables are taken at the freestream values as tabulated in Table-1.

Table-1: Freestream conditions

M_∞	$p_\infty \times 10^5$ Pa	T_∞ K
0.80	0.830	265
0.90	0.787	258
0.95	0.766	254
1.00	0.73	250
1.20	0.64	232
1.50	0.45	207
1.70	0.36	186
2.00	0.285	166
3.00	0.122	107

At a solid wall, the velocity tangential to the boundary is applied since the flow is inviscid. At transonic freestream Mach number, the computational domain of dependence is unbounded, and the implementation of boundary and initial conditions become critical, the known physically acceptance of far-field boundary conditions usually limit the flow

variables to asymptotic values at large distance from the payload fairing. Therefore, suitable coordinate stretching and placement of the far-field boundary condition have been considered in numerical simulations. The freestream conditions are prescribed on the outer boundary. For supersonic flow, all of the flow variables are extrapolated from the vector of conserved variables **U**. An image cell is imposed to the solved variables at the line of symmetry ahead of the vehicle.

2.4 Payload fairing Geometry and Computational Grid

Figure 2 shows geometry of the payload fairing having spherical-cone and cylinder. On the pitch and on the yaw planes nomenclature of pressure ports are $P_{\alpha 1}$, $P_{\alpha 2}$ and $Y_{\beta 1}$, $Y_{\beta 2}$, respectively, flush mounted pressure transduces. Pressure transducers are mounted at 0.77 D from the stagnation point of the payload fairing as depicted in Fig. 1. The maximum diameter of the payload shroud is D = 35 mm and the booster diameter is d = 8.75 mm. The spherical cap of the payload fairing is R = 8.75 mm. For the blunt-nosed cone, the inclination at the fore body is 20^{o}. The boat tail angle is measured clockwise from the axis with reference of the oncoming flow direction and is 15^{o}.

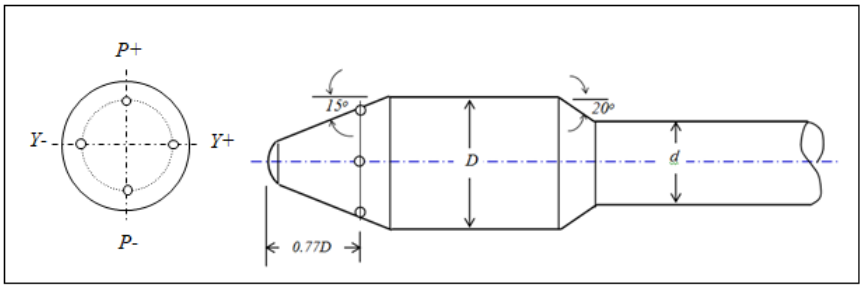

Fig-2: Geometrical detail of the payload fairing

2.5 Computational Grid

The body-oriented grids are generated using a homotopy one-to-one and onto technique in conjunction with finite element method [24]. The stretched grids are generated in an orderly manner. A non-uniform and non-overlapping structured computational cell is generated for numerical simulations. The grid-stretching factor is selected as 4, and the outer boundary of the computational domain is maintained as 3.5 − 4.5 times maximum diameter D of the payload fairing. In the downstream direction, the computational boundary is about 6 - 9 times the diameter of the module; D. The computational domain depends on freestream Mach number. Figure 3 shows three-dimensional view of grid over the payload fairing. The grid arrangement is found to yield a relative difference of about ± 3% in the pressure peak, which is in the same range as the stagnation pressure measurement error in the wind-tunnel. The convergence criterion is based on the difference in density values at any of the grid points, between two successive iterations $\left|\rho^{n+1} - \rho^{n}\right| \leq 10^{-5}$ where n is time-step counter. The numerical computations were carried out with various grid arrangements in order to meet a grid independency check. Grids typically contained 46 cells in the longitudinal direction, 45 cells in the transverse direction, and 15 – 25 cells in the body-normal direction. The minimum grid size in the normal direction of the payload fairing is about 1.70×10^{-4} m. The internal grid cells were constructed so that all of the nose pressure ports coincide with the center of a finite volume cell face.

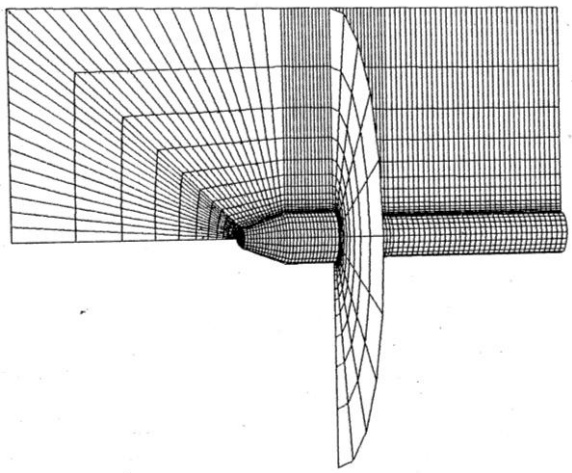

Fig-3: Computational grid over the satellite launch vehicle

2.6 Flowfield and surface pressure

The 3D Euler code was developed by us and used to simulate flow over the payload fairing. The code is second-order time accurate; the flow around the payload fairing is instantaneously steady at all points in flight. The assumption is reasonable, since only small changes in flow conditions occur over the time required for full development of the flowfield. It is important to mention here that the assumption allows the generation of CFD flow solutions at any point on the trajectory, independent of previous flight conditions. Simulations of the flowfield over the payload fairing were performed at various angles of attack and flight

conditions. The numerical calibration procedure produced results of comparable accuracy to that obtained by procedures which are well comply with wind tunnel data.

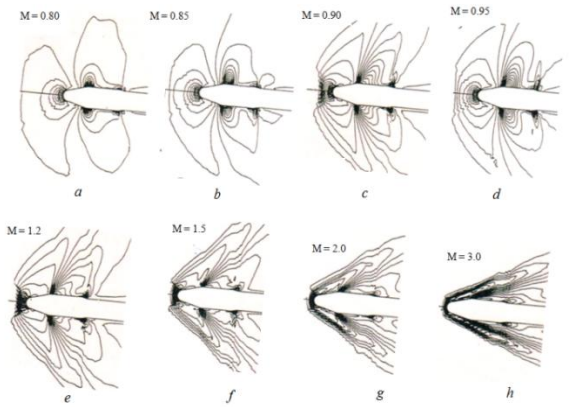

Fig-4: Density contours (a) – (d) transonic and (e) – (h) supersonic Mach numbers

Numerical simulations are carried out for flight Mach numbers of 0.5 to 3.0 at an increment of angle of attack $\Delta\alpha = 0.25^o$. Figure 4 shows the density contours at various M_∞ at $\alpha = 8^o$. It can be seen from the density contours that the flowfield characteristics depend on flight Mach numbers. The density contours in Fig 4 (a) - (d) exhibit the transonic flow behaviour of flowfield over the payload fairing. The terminal shock moves downstream on the payload fairing for $M_\infty < 1$. Figure 4 (e) – (h) shows formation of bow shock over forebody and presence of weak oblique shocks downstream of the cone-cylinder junction of the payload fairing for $M_\infty > 1$. The expansion and compression on the shoulder points of the payload fairing are visible in the density contours.

The pressure coefficient $Cp = [(p_o - p_\infty)/q_\infty]$ at the stagnation point is shown in Fig. 5 where p_o is the stagnation pressure, p_∞ is freestream pressure and q_∞ is freestream dynamic pressure. Stagnation point pressure coefficient is compared with wind tunnel results. The comparison shows good agreement between them. It can be seen from Fig. 5 that the stagnation point pressure coefficient increases with increase of M_∞.

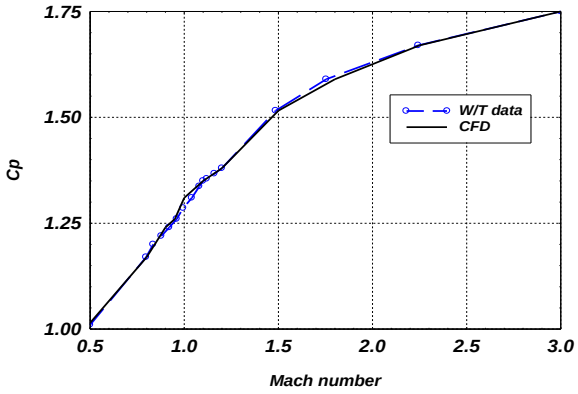

Fig-5: Variation of stagnation pressure coefficient

2.6 Local load variations

The probe pressure orifice locations were selected based on local structural load and under no flow separation condition in that region. At each station $Cp(\theta)$ was integrated circumferentially to obtain the aerodynamic load using numerically integrated following relation:

$$S\left(\frac{dCN_\alpha}{dx}\right) = 2\pi r(x)\int_0^\pi Cp(\theta)\cos\theta d\theta \cdots\cdots\cdots (5)$$

Where CN is normal force coefficient and S is reference surface area based on booster diameter d. Local normal force are computed at various locations using numerically computed coreferential pressure distribution. Table 2 shows the local normal force at different section in the conical region. We have selected x/D = 0.77 for mounting pressure transducers as shown in Fig 6(a). This location experience maximum normal pressure load. Figure 6(b) displays corresponding flush air data system employed in the estimation of angle of attack and sideslip angle. where subscripts α_1 and α_2 represent windward and leeward of the pitch plane and β_1 and β_2 in the yaw plane as shown in Fig 6(a).

Table-2: Aerodynamic local load in the blunt-cone section

M_∞	x/D				
	0.770	0.808	0.862	0.916	0.969
	$S(dCN_\alpha/dx)$ meter/radian				
0.75	1.1079	1.1202	1.1391	1.1174	1.1111
0.80	1.1123	1.1240	1.1340	1.1163	1.1127
0.90	2.2584	2.2830	2.3086	2.2729	2.2629
0.95	3.6839	2.8492	1.5064	1.4831	1.4780
0.98	4.7583	4.2970	1.7397	1.1316	1.1293
1.00	4.3782	3.8112	3.0857	3.0393	3.0314
1.20	6.4952	6.4523	5.4678	5.9781	6.2898
1.40	5.8570	6.1001	6.2525	6.6568	6.8331
1.60	5.7801	6.0293	6.3751	6.6840	6.9891
1.80	5.6287	5.8854	6.1946	6.6056	6.8521
2.00	5.4778	5.6875	6.0454	6.4937	6.7261
2.50	5.1435	5.3380	5.5820	6.0929	6.3973
3.00	4.8462	5.0000	5.1203	5.5933	6.0209

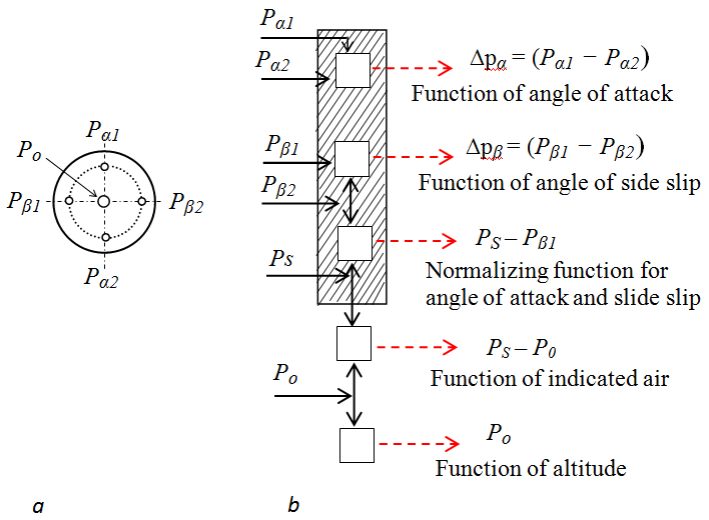

Fig-6(a): Location of pressure ports and (b) Flush Air Data System

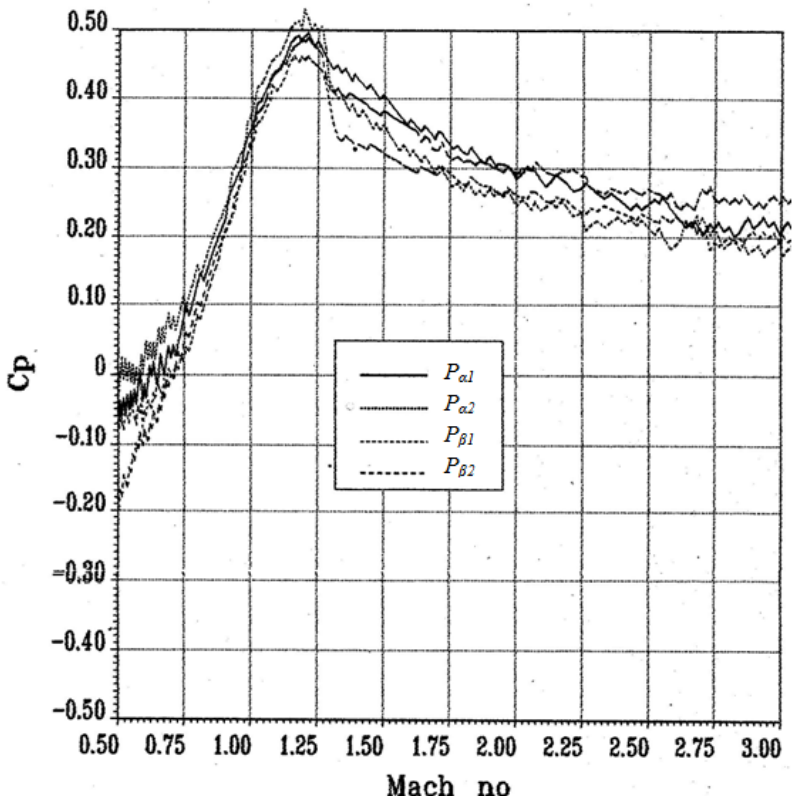

Fig-7: Measure Pressure coefficient at x/D = 0.77

Figure 7 displays the measured pressure at different ports ($P_{\alpha 1}$, $P_{\alpha 2}$, $P_{\beta 1}$ and $P_{\beta 2}$) at x = 0.77 D where x is measured from the stagnation point of the payload fairing. These pressure measurements are used to validate the location of pressure transducers and constructing the calibration charts for inverse analysis.

3. INVERSE PROBLEM

Calibration parameters are derived using computed ΔCp with small increment of M_∞ and α and β. The calibration factors span $0.5 < M_\infty < 3.0$ which covers maximum dynamic pressure and transonic region of the vehicle. The calibration factors are prepared help of the present numerical results. The differential pressure, Δp_α and Δp_β, are highly linear with respect to α and β, respectively. A controlled random search (CRS) method is used to estimate the angle of attack and sideslip angle from the measured transient differential pressure history during the ascent period of the launch vehicle.

3.1 Differential pressure measurement

The digitization of the flight pressure data is in 252 counts for the full scale range resulting in a data

error of 0.41×10^3 Pa for absolute pressure and 0.1096 $\times10^3$ Pa for differential pressure. Rosemount model [25] 1221F2AF of differential pressure transducer of range 17.23 – 172.36×10^3 Pa(d) (2.5 - 2.5 psid). sensitive coefficient k_1 and k_2 are 0.6 - 0.4. Telemetry requirement uses equipment bay (EB) to ground pressures of about 10 Hz response and two power monitoring FFT of pressure data is also needed to filter out unwanted frequencies.

Roll angle relates the orientation of the vehicle relative to the Earth's surface, and does not directly affect surface pressure or aerodynamics. The differential pressure in pitch and yaw plane are linear function of angle of attack. In order to obtain flow direction from these calibration factors, the equations are inverted to get $\alpha = \Delta Cp_\alpha/k_1q_\infty$ and $\beta = \Delta Cp_\beta/k_2q_\infty$ and $\alpha_t = \sqrt{(\alpha^2 + \beta^2)}$, where k_1 and k_2 are calibration constant and subscript ∞ represent freestream condition.. The flight data for the FADS were available from the vehicle telemetry system. The time history of the differential pressure is shown in Figure 8. The flight data represents the measured differential pressure in pitch Δp_α and yaw Δp_β planes. The differential pressure data sample rate was 10 samples per second. Figure 9 shows variation of Mach number with flight time of the vehicle. In estimation of α and β, one minimizes

$$F(V) = \left|D_C(\Delta\alpha.\Delta\beta) - D_M(\Delta\alpha.\Delta\beta)\right| \quad \ldots\ldots\ldots\ldots (6)$$

Where D_C and D_M are, respectively, the calculated and measured differential pressure at x/D = 0.77.

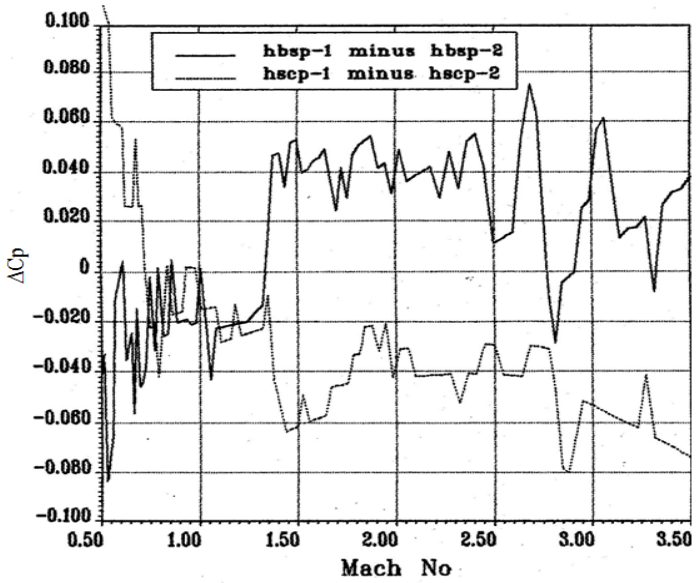

Fig-8: Measured differential pressure at x/D = 0.77

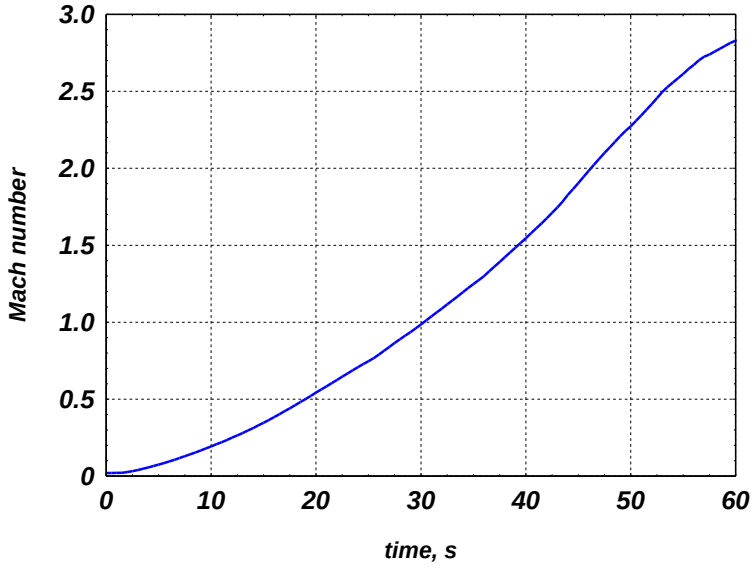

Fig-9: Variation of Mach number with flight time

3.2 Controlled Random Search Optimization Method

The CRS algorithm [26], an effective tool for global optimization, does not need computation of derivatives but depends on function F(V) evaluation alone. It works even when the differentiability requirements cannot be assured in the feasible domain of variable. For initiating this algorithm no initial guess value, except for an estimate of V, is needed.

A procedure for solving for α and β unknown air data parameters is now presented. Given that differential pressure observations are available on the payload fairing. The quantity F(V) is the surface pressure measured by sensor, and represent the unknown air data parameters which best fit the available set of pressure observations. For differential pressure sensors and solution require the inversion of an over constrained system.

The CRS algorithm does not need computation of derivatives but depends on function F(V) evaluation alone. The function F(V) is difference between measured and calculated values of the differential pressure. It works even when the differentiability requirements cannot be assured in the feasible region of variable. For initiating CRS algorithm no initial guess value, except for an estimate of α, β is required. The algorithm does not depend on the future-pressure information.

The CRS algorithm is implemented in two steps. In the first step, random feasible points generated from α, β and F(V) are computed at each point and information stored as a matrix. The maximum and minimum values $F_M(V)$, $F_L(V)$ of F(V) and corresponding points M and L are then identified. In the second step, these random points are manipulated iteratively to yield a better candidate for global solutions. To this extent at each iteration arbitrary distinct points are selected from matrix.

The CRS version works in two phases as mentioned by Mehta and Tiwari [27]. In the first phase, random feasibility points generated from V and F are evaluated at each point and the information is stored as matrix A. The maximum and minimum values F_M, F_L of F and the corresponding points M and L are then identified. In the second phase, these random points are manipulated iteratively to yield better candidate for global solution. To this extent at each iteration arbitrary distinct points are chosen from matrix A. A new point T = 2G – L, G being the centroid of these points, is generated and if T is in V, then F_T is evaluated. If $F_T < F_M$ then F_M and M in A are replaced by F_T and T. otherwise, T is discarded and a new T is generated. Treating any replacement as a success and setting the minimum success rate as 0.5, the efficiency of the procedure is enhanced by making use of the secondary trial Q = (3G – L)/4. If T or Q is a success, a third trial is also made with Y = 2.5 (T or Q) −1.5L and the best (with least F value) of T or Q or Y is used for replacement. The iteration process is continued till F_L falls below the prescribed threshold value.

The further details of CRS algorithm are described in the estimation of discharge coefficient by Mehta [28]. The estimated values of α and β are shown in Figure 10. A good agreement is found between estimated data with reconstructed flight trajectory employing post flight Inertial Measurement Units (IMU) data.

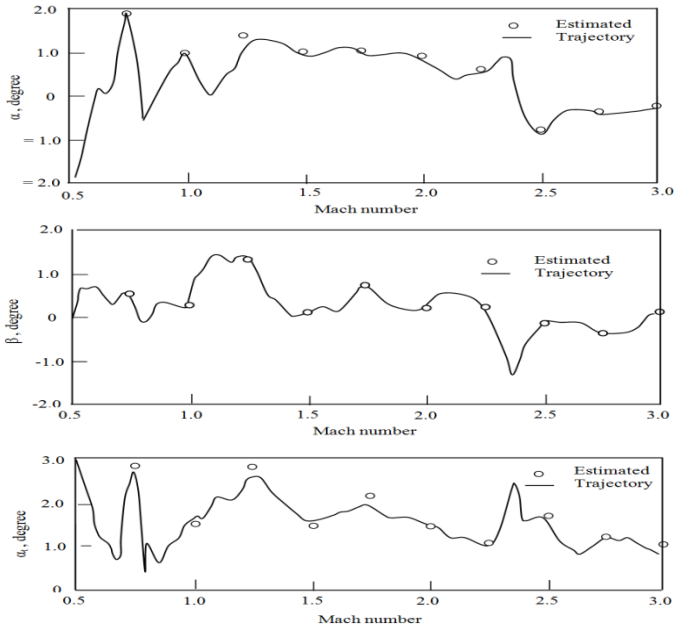

Fig-10: Comparison with reconstructed trajectory data

4. CONCLUSIONS

The code employs a three-dimensional finite volume space discretization to solve the integral form of the compressible inviscid equations over the satellite launch vehicle. A CRS method is used to estimate the angle of attack and sideslip angle from the measured transient differential pressure history during the ascent period of the launch vehicle. The algorithm predicts the α and β stepwise with function of Mach number. The predicted values of α and β are found to be consistent with the reconstructed telemetry data (IMU) as a function of the flight Mach number and found in reasonably good agreement.

REFERENCES

1. Liepmann, H. W., & Roshko, A. (2007). Elements of Gas Dynamics, First South Asian Edition, Dover Publications, Inc., India.
2. Larson, T. J., Moes, T. R., & Siemers III, P. M. (1990). Wind-tunnel investigation of a flush airdata system at Mach numbers from 0.7 to 1,4, NASA TM 101697, NASA Ames Research Centre California, USA.
3. Hillje, E. R., & Nelson, R. L. (1983). Ascent air data system results from the space shuttle flight test program, NASA CR 2283.
4. Watanabe, S., Ishimoto, S., & Yamamoto. Y. (1997). Aerodynamic characteristics evaluation of hypersonic flight experiment vehicle based on flight data, Journal of Spacecraft and Rockets, 34(4), 464-470. https://doi.org/10.2514/2.3259
5. Whitmore, S. A., Cobleigh, B. R., & Haering, E. A. (1998). Design and calibration of the X-33 Flush airdata sensing (FADS) system, NASA TM 206540.
6. Cobleigh, B. R., Whitmore, S. A., Haering, Jr., E. A., Borrer, J., & Roback, V. E. (1999). Flush air data sensing (FADS) system calibration procedures and results for blunt forebodies, AIAA 99–4816. https://doi.org/ 10.2514/6.1999-4816
7. Johnston, I. A., Tuttle, S. L., Jacobs, P. A., & Shimoda, T. (1999). The numerical and experimental simulation of hypervelocity flow around the HYFLEX vehicle forebody, Shock Waves, 9, 57–67. https://doi.org/10.1007/s001930050139
8. Davis, M. C., Pahle, J. W., Marshall, L. A., Mashburn, M. J., & Franks, R. (2000). Development of a flush air data sensing system on a sharp-nosed vehicle for flight at Mach 3 to 8, AIAA 2000-0304. https://doi.org/10.2514/6.2000-504
9. Fan, H.-Y., Lu, W., Xi, G., & Wang, S. (2003). An improved neural network based calibration method for aerodynamic pressure probes, Journal of Fluids Engineering, 125(1), 113-120. https://doi.org/10.1115/1.1523063
10. Rohlf, D., Brieger, O., & Grohs, T. (2004). X-31 vector system identification-approach and results, AIAA-2004-4830. https://doi.org/10.2514/6.2004-4830
11. Samy, I., Postlethwaite, I., Gu, D. W., & Green, J. (2010). Neural-Network-Based Flush Air Data Sensing System Demonstrated on a Mini Air Vehicle, Journal of Aircraft, 47(1). https://doi.org/10.2514/1.44157
12. Baumann, E., Pahle, J. W., Davis, M. C., & White, J. T. (2010). X-43A Flush Air Data Sensing System Flight–Test Results", Journal of Spacecraft and Rockets, 47(1), 48–61.
13. Paces, P., Draxler, K., Hanzal, V., Censky, T., & Vasko, O. (2010). A Combined Angle of Attack and Angle of Sideslip Smart Probe with Twin Differential Sensor Modules and Doubled Output Signal, IEEE Sensors Conference, Institute of Electrical and Electronics Engineers. DOI: 10.1109/ICSENS.2010. 5689866
14. Quindlen, J. F., & Langelaan, J. W. (2013). Flush air data sensing for soaring-capable UAVs, AIAA 2013-1153. https://doi.org/10.2514/6.2013-1153
15. Liu, Y., Xiao, D., & Lu, Y. (2014). Comparative study on a solving model and algorithm for a flush air data sensing system, Sensors, 14(5), 9210-9226. https://doi.org/10.3390/s140509210
16. Chen, G., Chen, B., Li, P., Bai, P., & Ji, C. (2015). Study on Algorithms of Flush Air Data Sensing System for Hypersonic Vehicle, Procedia Engineering, 99, 860-865. https://doi.org/10.1016/j.proeng.
17. Srivastava, A., & Meade, A. J. (2015). A Comprehensive Probabilistic Framework to Learn Air Data from Surface Pressure Measurements, International Journal of Aerospace Engineering, 1-19. http://dx.doi.org/10.1155/2015/183712
18. Karlgaard, C. D., Kutty, P., & Schoenenberger, M. (2017). Coupled Inertial Navigation and Flush Air Data Sensing Algorithm for Atmosphere Estimation, Journal of Spacecraft and Rockets, 54(1), 128-140.
19. Shevchenko, A. M., and Shmakov, A. S. (2017). Multi-Hole Pressure Probes to Wind Tunnel Experiments and Air Data Systems, Proceedings of the XXV Conference on High-Energy Processes in Condensed Matter, AIP Conf. Proc. 1893, 030088-1–030088-6. https://doi.org/10.1063/1.5007546
20. Reis, C. J. B., Manzanares-Filho, N., & de Lima, A. M. G. (2019). Robust optimization of aerodynamic loadings for airfoil inverse designs, J Braz. Soc Mech. Sci Eng, 41, 207. https://doi.org/10.1007/s40430-019-1705-z
21. Anderson, W., Thomas, J., & van Leer, B. (1986). A Comparison of Finite Volume Flux Vector Splitting for the Euler Equations, AIAA Journal 24(9), 1453-1460. https://doi.org/10.2514/3.9465
22. An, M. Y., Wang, K. C., & Tam, L. T. (1993). Computation of inviscid flow field around 3-D aerospace vehicles and comparison with experimental and flight data, AIAA 93-0885. https://doi.org/10.2514/6.1993-885

23. Bertin, J. J. (2006). Aerodynamics for Engineers, 4th Edition, Pearson Education in South Asia, New Delhi.
24. Mehta, R. C. (2017). Multi-block structured grid generation method for computational fluid dynamics, Scholars Journal of Engineering and Technology, 5(8), 387-393. Doi: 10.21276/sjet
25. Rosemount model, Aerospace Division, Rosemount Inc., Burnsville, Minnesota, USA, 1984.
26. Price, A. (2010). A controlled random search procedure for global optimization", Computer Journal, 26(4), 367-370. DOI:10.1093/comjnl/20.4.367
27. Mehta, R. C., & Tiwari, S. B. (2017). Controlled random search technique for estimation of convective heat transfer coefficient, Heat and Mass Transfer, 43(11), 1171-1177. DOI: 10.1007/s00231-006-0185-8.
28. Mehta, R. C. (2017). Analysis of payload compartment venting of satellite launch vehicle, Advances in Aircraft and Spacecraft Science, 4(4), 437-448. https://doi.org/10.12989/aas.2017.4.4.437